DOI: 10.13009/EUCASS2017-674

Detailed properties of iron oxide solid propellant catalyst

*F. Maggi *, S. Dossi *, C. Paravan *, L.Galfetti *, S. Cianfanelli ‡ and G. Marra §*

** Politecnico di Milano, Dept. Aerospace Science and Technology*

‡AVIO S.p.A., Colleferro, Italy

§Eni Donegani Research Center for Renewable Energies and Environment, Novara, Italy

Abstract

Hematite represents the most common burning rate modifier used in propellant production. The effect of burning rate fine tuning is obtained even for amounts ranging below 1 wt% of the total composition. Different studies have evidenced a role in ammonium perchlorate dissociation while few data are available regarding its capability to enhance binder decomposition. The acceptance of such ingredient in an industrial environment is based mostly on the verification of few parameters relevant to catalytic action (namely, particle size, specific surface area). The complexity of the iron oxide panorama shows a wide set of features neglected in standard quality check but important for a detailed characterization. Such properties assist in defining a unique fingerprint of the material and can be used for detailed identification of batch-to-batch reproducibility, for new supplier qualification, or for improvement of basic knowledge. The present paper is an extract of a detailed characterization activity performed on different lots of nominally identical propellant-grade hematite. A subset of results is proposed to show some peculiar properties of the ingredients and some characterization methodologies specifically employed for the scope.

Nomenclature

a	pre-exponential factor (Vieille's law)
a_s	SSA-based mean particle diameter
D_{10}	number-weighted mean diameter
D_{32}	surface-weighted mean diameter
D_{43}	volume-weighted mean diameter
d(x)	diameter of the x percentile
$m_{\%}$	instantaneous normalized mass
n	exponent (Vieille's law)
p	pressure
R^2	coefficient of correlation
r_b	burning rate
$T_{on,i}$	onset temperature of the i-th peak
T_{end}	temperature at the end of a peak
Δm_i	mass increment associated to the i-th peak
ΔH_i	reaction enthalpy of the i-th peak
ρ	density

AP	ammonium perchlorate
DSC	differential scanning calorimetry
HTPB	hydroxyl-terminated polybutadiene
ICP	inductive coupled plasma
SEM	scanning electron microscopy
SSA	specific surface area
TG	thermogravimetry
XPS	X-ray photoelectron spectroscopy
XRD	X-ray diffraction
XRF	X-ray fluorescence

1. Introduction

Iron oxide (Fe2O3, hematite) in solid propellants is commonly adopted as a ballistic modifier. In general, the role of iron oxide consists of tuning the ballistic properties of the propellant. The fraction of its use is quite negligible, in comparison to other ingredients (in the range of some fraction of percent to some percent) [

1] . The literature is rich of inhomogeneous data about the effect of the catalyst and, as a general conclusion, its action is strongly dependent on the composition under testing (specifically, the ions included in the oxidizer) and the

DOI: 10.13009/EUCASS2017-674

used fraction. In propellants based on ammonium perchlorate (AP), the effect is sensible and is rated up to about 100% of burning rate increment, within the entire pressure range [2]. However, this effect is obtained when a limited hematite fraction is used, ranging 1-5 wt.% in the whole propellant composition. Above such limit the burning rate decreases gradually. Several tests and configurations have been published by authors to understand the reasons of the catalyst action. The behavior of iron oxide with other oxidizers showed that, presumably, the effect is connected to the chlorine branch of the AP chemical activity. Other investigations underlined the coupled aspect of both homogeneous and heterogeneous effect. The action of a proton transfer mechanism is generally accepted. The fact is that a clear vision of the process is still lacking, even though the tests on oxides in general, and iron oxide specifically, started more than 50 years ago.

2. The iron oxide family

The chemical nomenclature lists 16 different types of iron-based oxides, hydroxides, or oxides-hydroxides. All these compounds are very common in the natural environment, most of them deriving from weathering of magmatic rocks and their further evolution. These molecules are formed mainly by combination of Fe and O ions, where the size of the O ion is much larger than the one of Fe. For this reason, the spatial displacement of oxygen imposes the crystal structure. In these compounds iron is found in the two valence states Fe(II) or Fe(III) providing tetrahedral or octahedral linkages. In nature, the only available arrangements in the third dimension of the anions are cubic close packing (ccp) and hexagonal close packing (hcp). The organization of atoms into crystals is stable from an energetic viewpoint. This grants a high energy of crystallization, favoring in most of the cases the generation of fine particles, reaching specific surface areas larger than 100 m2/g [3]. If we strictly limit the analysis to the “Iron Oxide”, both Fe(II) and Fe(III) oxides can be found (see Table 1).

Table 1: Summary of iron oxide properties

	Molar mass	**Specific gravity**	**Melting temperature,**	**Structure**
$\alpha - Fe_2O_3$ (hematite)	159.69 g/mol	5.26	1565 °C	hexagonal close-packing (Alternative: cubic close-packed)
$\beta - Fe_2O_3$	159.69 g/mol	N.Av.	N.Av.	N.Av.
$\gamma - Fe_2O_3$ (maghemite)	159.69 g/mol	4.87 [4]	N.Av.	Inverse spinel
$\epsilon - Fe_2O_3$	159.69 g/mol	N.Av.	N.Av.	N.Av
Fe_3O_4 ($Fe^{II}Fe_2^{III}O_4$, magnetite) [5]	231.54 g/mol	5.18	1590 °C	Inverse spinel
FeO (wüstite)	71.84 g/mol	5.72-5.61	1377 °C	two interpenetrating face-centered cubic structures

- The $\alpha - Fe_2O_3$ is the most stable form of iron oxide. It is amphoteric, paramagnetic, and has a blood-red color if finely grinded. It has a hexagonal close-packing structure. Iron ions are in the octahedral interstices (corundum). The unit cell of the crystalline structure is composed by six formulas. In the literature, an alternative cubic close-packed structure is also known, if mild oxidation of Fe_3O_4 is provided.
- The $\gamma - Fe_2O_3$ has a red-brown color. It is ferromagnetic. As the magnetite, it has an inverse spinel structure with cation-deficient sites. It can be found in nature as a weathering product of magnetite-based minerals. It can also be produced by heating of other oxides, mainly in presence of organic substances. Commercial maghemite has a tetragonal structure and derives from a process involving phase transformations.
- Both the $\beta - Fe_2O_3$ and the $\epsilon - Fe_2O_3$ are synthesized only in laboratory under specific operating conditions. The β phase was obtained by the controlled de-hydroxylation of $\beta - FeOOH$ under vacuum at

DOI: 10.13009/EUCASS2017-674

the temperature of 170 °C. The ϵ can be prepared in different ways but it turns to hematite if heated to 500-750 °C. Its structure is preparation-dependent and it can be identified as one of the intermediates when turning hematite to magnetite.

- The Fe_3O_4 is an amphoteric oxide, resulting from the combination of the oxidation states Fe(II) and Fe(III), arranged in mixed octahedral/tetrahedral sites (inverse spinel). The crystalline unit cell is face-centered cubic based on 32 oxygen ions. Magnetite is featured by ferromagnetic properties and high electric conductivity.
- Finally, the FeO crystal unit cell is based on 4 formula units. The material is unstable at room temperature unless fast cooling is performed. In this case a metastable condition obtained. In general, this iron oxide does not exist under the nominal composition, as a cation-deficient phase is likely to be present. The real chemical formula results in Fe1-xO, with x ranging between 0.83-0.95.

3. The catalytic action

The main iron oxide catalysts used in industrial applications are magnetite and hematite. Both are amphoteric so they can be used in either acid or basic catalysts, in oxidation/reduction chemical processes. It was observed that the performance of the material depends from the specific surface area. For this reason, most of these materials are nanometric (from few hundreds of nanometers down to few nanometers). In this respect, the efficacy of the dispersion and the position with respect to the main reactant play a significant role. Results in this direction are obtained for AP/hematite mixtures by Ma and co-authors. In their work the improvement of AP decomposition action is obtained when proximity between AP and the iron compound is obtained by the production of AP/Fe2O3 composites [6].

Within the list of the reactions involving iron oxide catalysis we can find ammonia generation from hydrogen/nitrogen reaction, dehydrogenation of some hydrocarbons, high-temperature water/gas shift reaction (CO+H2). It appears that the action is obtained when hydrogen molecules are involved and, so, proton transfers. A complete overview is reported in a review book by Cornell and Schwertmann [3].

Studies on the role of catalysts in the decomposition path of ammonium perchlorate are abundant in the literature, if hematite is considered. In thermogravimetric studies of AP and iron oxide mixtures an anticipation of the decomposition reaction onset is obtained for the oxidizer. As expected, no change occurs in phase transition. Joshi and co-authors published a paper about the activity of nanometric oxide [7]. They tested different mass fractions with three sizes (30 µm, 30 nm and 3.5 nm), showing that the micrometric iron oxide does not lead to significant improvements while the anticipation of the decomposition peak is clearly visible as the finer oxide powders are used.

Few data are available for the catalysis of other iron oxides on ammonium perchlorate. About magnetite, the effect of particle shape and concentration has been investigated by Wang and Yao [8]. Magnetite demonstrated to be an effective decomposition catalyst, anticipating both the onset of the main decomposition reaction and the offset of the mass sublimation. As expected, the reactivity is dependent from both shape and size of the powders. Basically, this cross influence suggests that the dominating parameter is represented by the specific surface area of the samples. Another work by Oyumi focused on the comparison between magnetite and hematite catalytic actions. The reference energetic material was an azide propellant containing ammonium perchlorate. Tests have demonstrated that, under such operating conditions, magnetite performs better in terms of decomposition onset and offset [9]. Moreover, propellants feature a lowered pressure exponent.

The decomposition of the binder is rarely addressed in the open literature. There are several mentions in papers regarding propellant studies (e.g. Chakravarthi et al. [2], Patil and co-authors [10]) but specific works about iron oxide effect on binder pyrolisis are lacking. Some information can be gathered from the literature relevant to hybrid rocket motor performance analysis. Frederick and co-authors reported the regression rate investigations of solid fuels made by an oxidizer-lean composition of AP and HTPB. Some of the formulations included also hematite as a catalyst. Experimental results evidenced the increment of regression rate in presence of AP and of AP/Fe2O3. The catalyst effect was more marked as the AP load was incremented [11]. Some information on polyurethane decomposition in presence of metal oxides only can be found in the literature about fire protection [12]. In a paper by Liu and co-authors the reduction of smoke and the increment of charring on the burning surface is obtained by adding hematite. In general metal cations, and iron (III) oxide specifically, are known to catalyze the generation of double bonds, supporting cross-linking during pyrolysis process and, for this reason, promoting the generation of porous char layer.

Finally, the reaction between iron (III) oxide and aluminum is known to generate a thermite process. In this specific case the reaction consists of an oxygen exchange between one oxide and a metal. The stoichiometric reaction is given in (1).

DOI: 10.13009/EUCASS2017-674

$$Fe_2O_3 + 2Al \rightarrow 2Fe + Al_2O_3 + Heat\ (\approx 850\ kJ) \quad (1)$$

The reaction has been extensively studied in the past, as it is very common in powder metallurgy. An ignition source is required to trigger the process. Then, self-propagation of the flame is obtained. The predicted adiabatic flame temperature is 3135 K. The onset of the reaction for nano-thermites is reported by Puszynski to be 565 °C [13]. A three-step reaction is identified, involving the generation of other iron oxides (Magnetite and Wustite) as intermediate products [14]. To date, it is not clear if such reaction may be present on the burning surface of a metalized propellant.

3. Identification and analysis

Iron (III) oxide represents the most used catalyst in rocket propulsion. Its crystal shape tends to be dependent from the environment where it grows and is sensitive to the presence of additives [3]. The most common attitude is rhombohedral, platy, and rounded, with various thicknesses. It can be produced by calcination or grown in solution, producing varying crystal shapes. The calcination technique is a convenient method but it is operated at 800-900 °C, causing the growth of the final particles. This type of hematite has a specific surface area of about 5 m^2/g. Other production techniques, such as the dehydroxylation of OH-based iron compounds at 500-600 °C, enable the generation of particles having a specific surface area of about 200 m^2/g. Alternatively, a solution-based production methodology can grant a specific surface area in the range 15-90 m^2/g.

Magnetite typically takes mainly an octahedral shape. However, also in this case, the processing and the composition can alter the final crystal shape. For example, round shapes may be obtained by slow oxidation. The expected specific surface area of the powder ranges between 4 and 100 m^2/g, depending on the production technique.

Maghemite does not have a peculiar shape. The reason stands in the fact that the material is obtained from other oxides. For this reason, the final shape of a crystal inherits the aspect of the original material. In the competent literature, different sources report a specific surface area of the powder between 8 and 130 m^2/g, depending on the production technique.

The role of iron oxide during combustion can be assimilated to a heterogeneous catalysis, being based on a solid-gas interaction. In this respect, this kind of process is very much dependent from the surface properties of the material, including porosity. In addition, per the size scale, the heterogeneous interaction at the interface may be perturbed by the electronic structure if the typical catalyst dimension is 10 nm or smaller. If larger, the interaction is mostly influenced by the surface properties [15].

Laser diffraction techniques can be used for the initial assessment of particle sizes but the methodology becomes difficult to perform when the size decrements in the nanometric range due to dispersion issues. The nitrogen adsorption has been used to characterize the properties influencing the catalytic action [16]. In this case, the measurement of the specific surface area (using Brunauer-Emmett-Teller approach) can be the sole method for the characterization, unless a statistically-weak one-to-one particle measurement is performed using SEM micrographs. From the reactivity viewpoint, the most used methodology consists in the application of thermal analysis techniques. Differential thermal analysis or differential scanning calorimetry, coupled with thermogravimetry, are very often used to understand the behavior of the iron oxides with samples.

The characterization of the material inner structure can be performed by spectroscopic methods. The X-ray diffraction technique identifies the crystalline structure of the matter. It demonstrated to be effective in the field of inorganic compounds where an ordered arrangement of atoms is present. Amorphous matter state cannot be properly identified. High energy of crystallization of iron oxides may suggest a preferential crystalline, rather than amorphous state, enabling the proper identification with this technique. Distinctive refraction patterns are known for all iron-derived compounds and polymorphs. The IR spectroscopy was observed to be valid also for those materials that were too thin for XRD analysis. Crystal morphology, degree of crystallinity, metal substitutions and other features can be identified by the shift of the peaks in the absorption spectrum. It is interesting to note that not all X-ray techniques are valid for the characterization of bonds. In general, the X-ray photoelectron spectroscopy (XPS) has the capability of detecting both atom concentrations and the relevant bonds by interpreting the peak shifts. However, in the case of iron-based compounds this is not possible because the spectroscopic pattern of several iron oxides does not present a distinctive shape and the differences overlap. In this respect, the sensitivity of the sample to ultra-vacuum conditions should be considered. Crystal surfaces may feature relaxation or reconstruction. The former process consists of the shift of interatomic distances in the bulk and change of bond angle in the first and second layer. The latter consists in

DOI: 10.13009/EUCASS2017-674

the propagation of the change also in the nearest neighbors [3]. Finally, as in several chemical and metallurgical applications, the purity of the ingredient at ppm level may be assessed using Inductive Coupled Plasma. With the same scope, X-ray fluorescence (XRF) can be applied, ruling the intensity of the X-ray beam to identify either superficial species or bulk atomic concentrations [17].

4. Experimental characterization

The characterization of two space-grade iron oxides (ID Names A and B) are reported in this paper. The materials are nominally highly pure hematite, the exact grade being undisclosed for industrial reasons. Details of the experimental characterizations are given hereafter.

4.1 Scanning electron microscopy

SEM pictures were obtained by a JEOL JSM-7600F thermal field emission scanning electron microscope at 5 kV and several magnifications. Each powder was dispersed on a metal support provided with a conductive graphite-based bi-adhesive tape and mounted on a multi-sample holder. To improve image quality, a nano-layer of Cr with a Denton Vacuum DESK V sputter system may be applied.

The SEM images of the presented batches are reported in Figure 2 and Figure 1. Both exhibit the presence of micron-sized clusters, composed by nano-sized particles with a size ranging from 100 nm to 400 nm. Granules feature a smooth superficial texture but are not spherical. Elongated particles or objects like torpedoes are visible. The presence of exotic particles with internal holes or with an extremely irregular shape is also evident. The external surface is relatively regular evidencing the typical structure of a crystal. Flat planes can be seen for the smallest particles in the 50000x images, mainly in Figure 1.

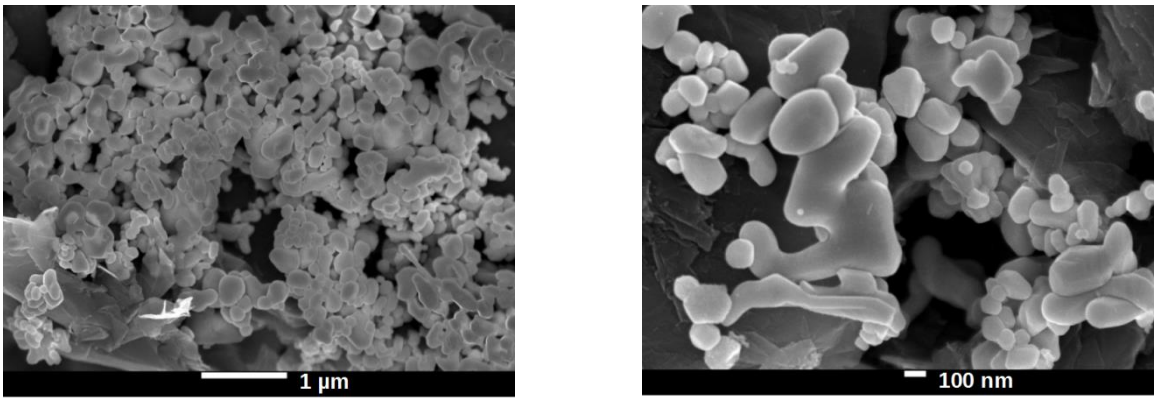

a) Magnification: 20000x b) Magnification: 50000x

Figure 1: SEM images of the sample A.

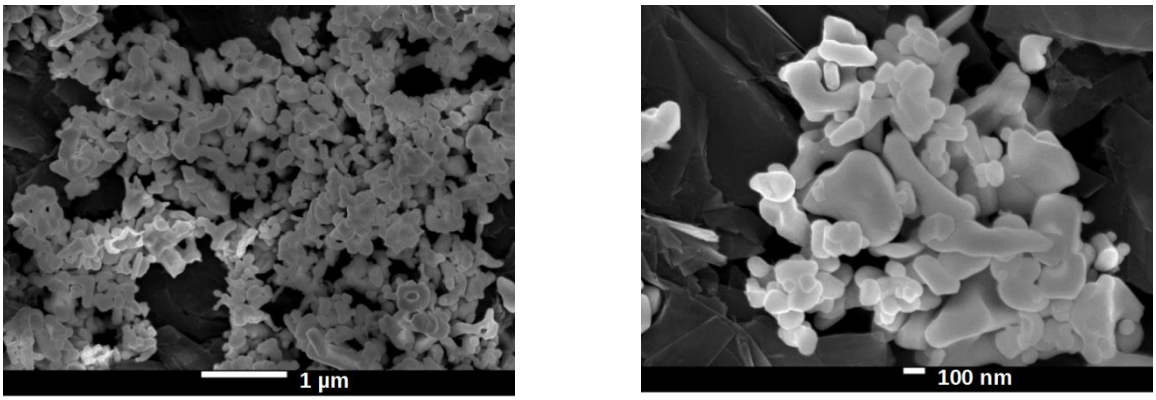

a) Magnification: 20000x b) Magnification: 50000x

Figure 2: SEM images of the sample B.

DOI: 10.13009/EUCASS2017-674

4.2X-ray diffraction

Analyses were executed by a PANalytical X'Pert alpha-1 Θ/2Θ X-Ray Diffractometer with Bragg-Brentano geometry. Preparation consisted in positioning and leveling a small amount of powder inside a sample holder. No powder pretreatments were necessary being the granules sufficiently small. Tests were executed using a radiation X Cu Kα (λ = 1.5416 Å) at 1.6 kW. The selected angular range was 5°-90° (2Θ) with a pass of 0.02° (2Θ) and an acquisition time of 15 s/pass. Search of identified inorganic phase was performed using the Hanawal method. The crystallite size has been determined only on hematite, looking at the peak spans.

The results of the analysis are reported in Table 2. Both samples show a predominance of hematite. The batch A shows the presence of a non-negligible amount of magnetite while the lot B did not show other crystalline phases. The size of the crystallite is almost similar to the size of the fine fraction of the powders, meaning that mono-crystal particles may be present. It should be noted that larger crystallite size is obtained for the batch containing the magnetite impurity. It is not clear if a correlation is present between these specific parameters.

Table 2: Crystalline composition and crystallite size of the tested iron oxide batches.

Batch Sample	**Recognized Phases**		**Crystallite size, nm**
	Fe_2O_3, %	**Fe_3O_4, %**	
A	97.3	2.7	240
B	100.0	0.0	170

4.3 Inductive coupled plasma

Analyses were executed through a Varian 710 ICP-OES. To perform the analysis the most intense emission line of the interested elements was selected verifying the absence of interference with the support matrix. Sample mineralization was performed using a water/turpentine+HF(10%+2) solution. The suspension was then microwave-processed. All the chemicals used for the solution preparation had a maximum impurity content of 1000 ppb.

Table 3: Impurities mass fraction detected by ICP-OES technique

Element	**Al**		**Ca**		**Na**		**Cr**		**Mn**	
Powder Batch	**U.M.: mg/kg**		**U.M.: mg/kg**		**U.M.: mg/kg**		**U.M.: mg/kg**		**U.M.: mg/kg**	
	Res.	***Unc.***	**Res.**	***Unc.***	**Res.**	***Unc.***	**Res.**	***Unc.***	**Res.**	***Unc.***
A	<10	± *5*	92	± *5*	108	± *10*	34	± *3*	954	± *30*
B	15	± *5*	263	± *5*	320	± *10*	12	± *3*	1443	± *30*

Element	**Ni**		**S**		**Si**		**Zn**		**Mg**	
Powder Batch	**U.M.: mg/kg**		**U.M.: mg/kg**		**U.M.: mg/kg**		**U.M.: mg/kg**		**U.M.: mg/kg**	
	Res.	***Unc.***	**Res.**	***Unc.***	**Res.**	***Unc.***	**Res.**	***Unc.***	**Res.**	***Unc.***
A	67	± *3*	301	± *20*	198	± *5*	94	± *3*	32	± *3*
B	48	± *3*	607	± *20*	136	± *5*	94	± *3*	75	± *3*

4.4 Particle size measurement

The particle size distribution was evaluated by Malvern Mastersizer 2000, with wet dispersion (Hydro 2000S). The instrument provides the particle size distribution data exploiting the laser radiation scattering caused by the disperse system when it is suspended in a dispersing medium and is moving through the test section. In the data reduction

DOI: 10.13009/EUCASS2017-674

approach, the size distribution is reconstructed assuming spherical and smooth-texture particles. The difference between the instrument sensor signals and the output particle size distribution is expressed in terms of percent weighted residuals. In this analysis, tests with weighted residuals > 5% were rejected. Two different data fitting models were adopted to produce the final outputs. The first one is a general-purpose model based on a broad particle size distribution (WD). The second data reduction approach considers a specialized fitting that emphasizes the presence of different peaks in the powder particle size distribution (BD). The BD approach is implemented to evaluate the possibility of capturing some peculiarities of the captured scattering signal that are not fully caught by the WD. The iron oxide powders were dispersed in bi-distillated water. Nonidet P-40 was used as dispersant. During the analysis, the same iron oxide sample was measured multiple times. Thanks to the embedded stirring system, hydrodynamic stresses exerted by the suspending medium on the sample particles promoted the rupture of the (eventually present) clusters. A minimum of two reproducible tests were achieved for each lot.

Results reported in Table 4 show two sub-micrometric powders, with similar particle distribution properties. The d(0.1) settles close to range of the crystallite size. Both the mass-mean and the surface-mean diameters are sub-micrometric and the d(0.9) is slightly above one micron. Both WD and the BD model reflect similar condensed parameters.

Table 4: Particle size distribution relevant and fitting parameters; WD model.

Id.	d(0.1) μm	d(0.5) μm	d(0.9) μm	D_{32}, μm	D_{43}, μm
A	0.358	0.758	1.430	0.613	0.850
B	0.301	0.638	1.219	0.528	0.725

Table 5 Particle size distribution relevant and fitting parameters. BD model.

Id.	d(0.1) μm	d(0.5) μm	d(0.9) μm	D_{32}, μm	D_{43}, μm
A	0.416	0.559	1.456	0.628	0.801
B	0.400	0.506	1.353	0.565	0.705

4.5 Specific surface area determination

The powder SSA is determined by the Brunauer-Emmet-Teller (BET) approach [18] based on low temperature (77 K) adsorption and desorption of N_2. The experimental setup is a Micrometrics ASAP 2000. The tested samples are pre-treated by a degas process performed for 3 hours at 300°C. The SSA data are reported in Table 6, and are completed by the indication of the volume of the surface pores. The mean particle diameter computed through the SSA information is smaller than the one obtained by the laser scattering technique but they are close to the crystallite size.

Table 6 Specific surface area (SSA), SSA-based mean particle diameter, and pore volume of the tested iron oxide batches.

* SSA-based mean particle diameter, $a_s = \frac{6}{SSA \cdot \rho_{\alpha-Fe2O3}}$

Id.	SSA, m^2/g	a_s^*, nm	Pore Vol., cm^3/g
A	6.3 ± 0.1	182	0.02 ± 0.01
B	7.2 ± 0.1	159	0.03 ± 0.01

DOI: 10.13009/EUCASS2017-674

5. Initial assessment of reactivity

The iron oxides have been characterized as catalysts inside propellants and slurries having relevant compositions like the one used in the final application. The nominal compositions are reported in Table 7. All preparations have been performed using the same batch of raw materials, except for iron oxide.

Table 7: Tested propellant compositions

Ingredient (Short hand notation)	Baseline wt %	With hematite wt %
Ammonium Perchlorate (AP)	68.00	67.72
Micrometric aluminum	18.00	18.00
HTPB	14.00	14.00
Iron Oxide	No catalyst	0.28

5.1 Thermogravimetric tests on propellant slurries

Simultaneous thermal analyses based on differential scanning calorimetry (DSC) and thermogravimetry (TG) were performed by Netzsch Jupiter 449 F5. The runs are conducted in Ar (mass flow rate 70 ml/min), with heating rate of 10°C/min. The investigated temperature range extends from 30°C to 1100°C. Tested samples have a mass of (3.0 ± 1.0) mg. Two repeatable runs were achieved for each formulation (i.e, differences on the onset temperatures < 10%). The investigated propellant formulation is reported in the Table 7, manufacturing was performed by resonant acoustic mixing [19] under vacuum (0.1 bar, 20-30 g acceleration). The reactivity of the different tested materials is evaluated considering the TG trace. In particular, onsets and ends of the reactions involving mass changes are evaluated according to the tangents method [20]. The typical result achieved by a DSC-TG run for the baseline formulation without iron oxide, is reported in the Figure 3(a). The DSC-TG of a propellant slurry containing hematite is presented in Figure 3(b). Under the investigated conditions, the reduced sample mass may induce problems of uniformity (e.g., heterogeneous composition with different mass fraction with respect to those of the bulk propellant presented in the Table 7). Nevertheless, the considered approach is consistent with open-literature analyses [10]. Moreover, due to the reduced size of the tested hematite powders, additive dispersion may yield significant contributions to the data scattering between different runs.

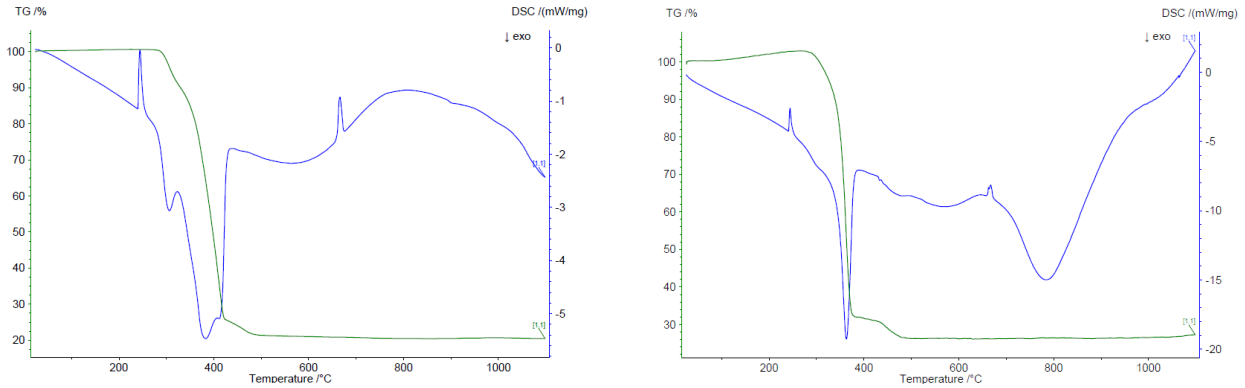

a) Baseline (no iron oxide) b) Sample curve with hematite (lot B)

Figure 3 DSC-TG run for propellant slurries
Tested condition: Ar (70 ml/min), 10°C/min, 30-1100°C.

DOI: 10.13009/EUCASS2017-674

Table 8 DSC-TG data for the tested propellant slurries (Ar, 70 ml/min, 10°C/min, 30-1100°C). reactivity parameters are identified as the average values over two reproducible tests, uncertainties are defined by standard deviation. Data scattering is mainly influenced by the ingredients dispersion in the propellant slurry.

$$* \Delta m_{\%} = {(m_{\%,\,On} - m_{\%,End})}\Big/{(T_{On} - T_{End})}$$

[a] Single run data available

Id.	Baseline	P-A	P-B
$T_{on,1}$, °C	360.8 ± 1.5	347.4 ± 1.8	346.6 ± 1.1
Δm_1, %	-61.8 ± 6.7	-65.0 ± 5.9	-73.1 ± 1.9
ΔH_1, kJ/g	1.51 ± 0.04	2.13 ± 0.41	2.27 ± 0.01
$T_{on,2}$, °C	437.9 ± 1.8	435.3 ± 4.8	431.3 ± 0.7
Δm_{1+2}, %	-67.1 ± 7.4	-74.0 ± 5.6	-77.7 ± 2.1
ΔH_2, kJ/g	0.42 [a]	0.43 ± 0.17	0.14 ± 0.02
$\Delta m_{\%,1}$*, %/°C	1.26 ± 0.03	2.73 ± 0.16	3.28 ± 0.52

Considering the data presented in the Figure 3, the first endotherm with peak at 244°C corresponds to the orthorhombic to cubic phase transition of AP. After this, an exothermic process starts (AP and HTPB decompositions). The onset of this latter reaction occurs at $T_{on,1}$ = 359.7°C, and it yields a mass change Δm_1 = -66.9%. The end temperature of the reaction is $T_{end,1}$ = 419.3°C. This decomposition is followed by a second reaction with $T_{on,2}$ = 437.1°C, $T_{end,2}$ = 480.6°C, and Δm_2 = -5.7%. The enthalpy release in the two decompositions steps (as evaluated by the DSC trace) results ΔH_1 = 1.54 kJ/g, and ΔH_2 = 0.5 kJ/g respectively. The following reaction is the Al melting with an onset at 660.8°C. An overview of the results achieved when testing propellants with the iron oxide is reported in the Table 8.

As expected, the iron oxide exerts no influence on the AP phase transition [10], while it lowers the onset temperature for the AP + HTPB decomposition (see $T_{on,1}$ in Table 8). The baseline propellant shows $T_{on,1}$ = (360.8 ± 1.5)°C. The formulation loaded with iron oxide from the lot A reduces the onset temperature to (347.4 ± 1.8)°C. On the other end, no marked difference can be noted when comparing the other iron oxide lots (see Table 8). The addition of the catalyst promotes an increase in both the propellant decomposition (Δm_1) and its enthalpy release (ΔH_1). In terms of the AP + HTPB decomposition, the batch B shows a reduced data scattering between the runs. This effect may result from a relatively easier dispersion of the catalyst of these batches, and sample composition homogeneity. The ΔH_1 shows a behavior like that of the Δm_1. Also in this case, the reactivity parameter change between the baseline and the iron oxide loaded formulation is evident, and the lot B shows a reduced data scattering with respect to the other formulation. When considering the overall mass change (Δm_{1+2}), the data reported in the Table 8 show the absence of marked differences between the different samples, being the error intervals partially overlapped.

5.2 Propellant burning rate characterization

The experimental ballistic characterization was performed in a stainless steel horizontal strand burner of 2-liter volume equipped with 2 optical accesses for propellant combustion video recording. Combustion tests were executed at different pressures in nitrogen atmosphere to avoid propellant-environment interactions. The pressure was kept constant by a set of electrovalves controlled through an analog regulator and an external gauge. Hot wire ignition has been selected. The propellant was cut in samples of 4x4x30 mm side-inhibited by a solution of low molecular weight polymer to guarantee a flat flame front. A video camera linked to a personal computer recorded the propellant combustion. A scheme of the experimental rig is reported in Figure 4. For each interested pressure, at least 3 good videos were recorded and post processed by a proprietary software (HYDRA) capable of computing the average steady burning rate of the strand (carefully avoiding ignition and extinction transient effects). Finally, data were correlated through a standard Vieille law $r_b = ap^n$ where, "p" is the pressure, "a" and "n" are the fitting constants determined experimentally.

DOI: 10.13009/EUCASS2017-674

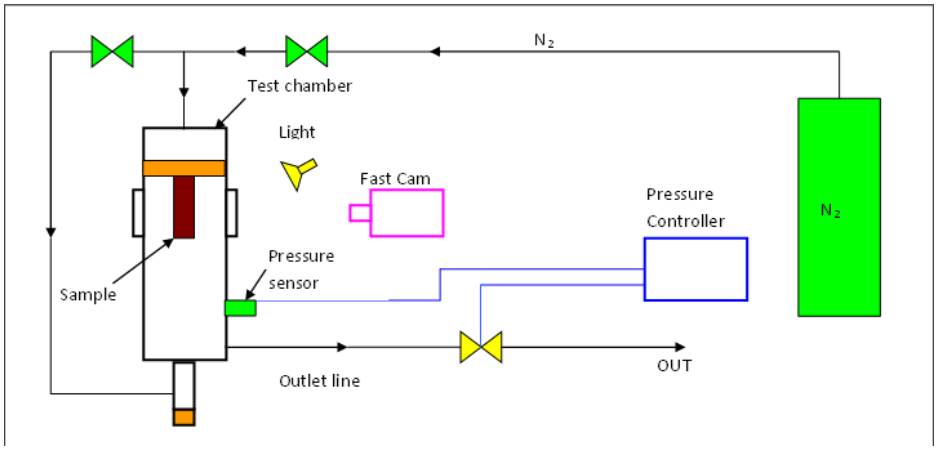

Figure 4: Scheme of the experimental rig for combustion tests

Table 9: Vieille's law of the tested propellants

Propellant Label	Line Color	Vieilles's law	R^2
P-A	Blue	$1.57\pm0.13p^{0.42\pm0.02}$	0.982
P-B	Green	$1.36\pm0.16p^{0.46\pm0.03}$	0.971

The result summary of the ballistic characterizations is reported in Table 9 while the plots of data fitting and burning rates at different pressures are reported in Figure 5. The direct r_b comparison confirms that, from a statistical point of view, there are no appreciable differences among the tested propellants. The propellant P-A is characterized by the lowest pressure sensitivity (n = 0.42) potentially causing r_b anomalies at high pressures. The other propellant features a pressure exponent of 0.46 - 0.47. Even in the point-to-point analysis of the burning rate, all data are statistically indistinguishable.

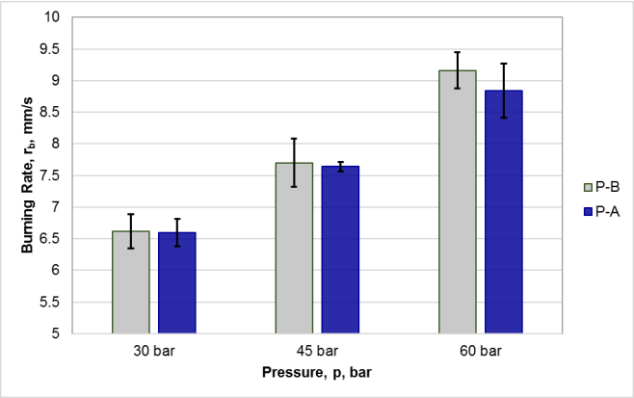

a) Detail

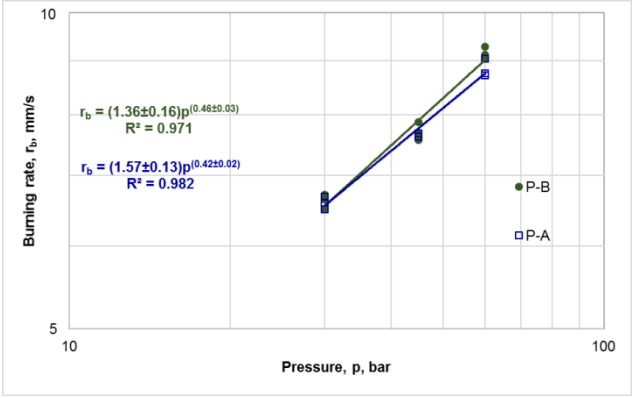

b) Power fitting

Figure 5: Burning rate of propellants containing iron oxide

DOI: 10.13009/EUCASS2017-674

5.3 • Propellant extinguished surfaces

This novel characterization consisted of the extinguishment of a propellant sample under burning conditions by depressurization below its deflagration limit and the analysis of the extinguished surface by using XRD techniques. The scope of the analysis consisted of the identification of the combustion intermediates residing on the burning surface.

Sample extinguishment was performed by pressure deflagration limit in a vertical combustion chamber with optical accesses. The volume of the chamber is about 40 liters filled with rarefied nitrogen. Vacuum pump is used to evacuate the chamber and produce low pressure. After ignition, the internal pressure is slowly decremented to ensure a quasi-steady combustion process, till the flame naturally extinguishes. Extinguishment pressure was not monitored. A scheme for the chamber assembly is reported in Figure 6.

Once the propellant was extinguished, the sample was analyzed using XRD. Tests have been performed with a powder diffractometer Philips X'Pert θ/2θ with two different configurations.

- With oblique beam having constant inclination ω of 1.0°, using X Cu K_α con λ=1.5416 Å emission and 1.6 kW power (visibility of 200-300 nm superficial layer).
- with Bragg-Brentano configuration, angular range 5 to 90° (2θ), steps 0.02° (2θ) and acquisition time of 15 second per step (sub-surface visibility).

Inorganic phases were identified with the search method Hanawalt on PDF-2 data set (Powder Diffraction File, ICDD). Examples of XRD patterns for both analytical configurations are reported in Figure 7 and Figure 8 for powder A. The quantitative analysis of both samples is reported in Table 10 and Table 11.

Different angles were attempted as well as samples having different cross-section area were supplied (from 4x4 mm^2 to 10x10 mm^2). In all tested configuration, the technique was not able to identify any iron oxide content. The elements observed by the XRD method in Bragg-Brentano configuration consisted of the original constituents of the propellant (ammonium perchlorate and aluminum), representing the bulk of the material. The oblique beam configuration was performed with the aim of analyzing the surface layer. For this measurement, an imprecise data uncertainty was expected because the extinguished region could not be represented by a Euclidean surface. In this last case, intermediates of AP reaction could be observed (ammonium chloride). It is realistic to consider that the amount of iron oxide (0.28 wt.%) is too small for a proper detection with XRD methodology.

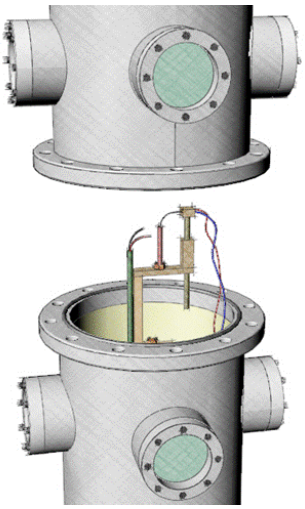

Figure 6 Scheme of the subatmospheric combustion chamber

DOI: 10.13009/EUCASS2017-674

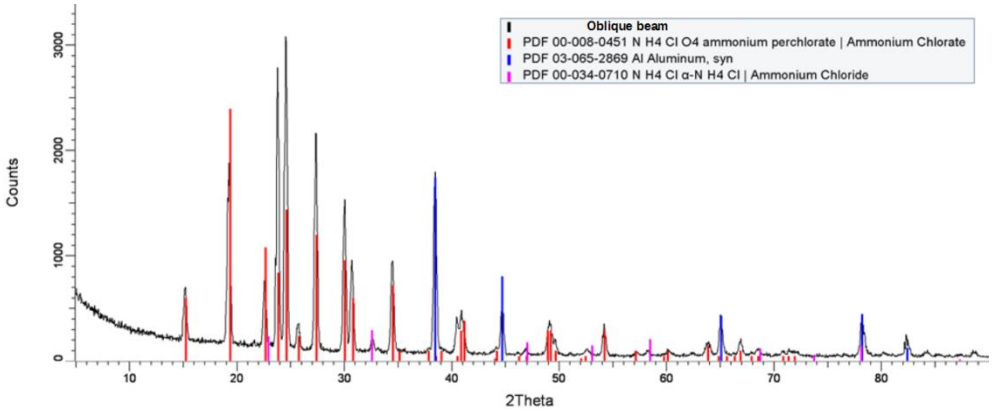

Figure 7: XRD analysis of extinguished surface of sample A. Oblique beam.

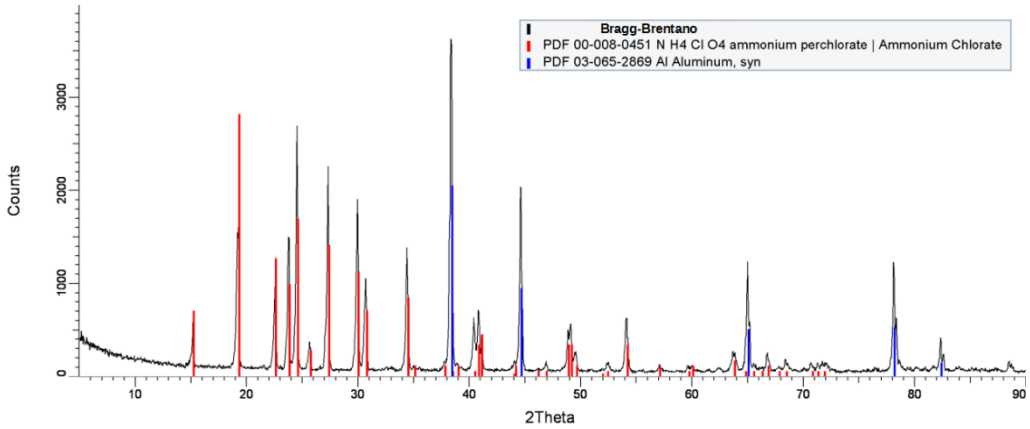

Figure 8: XRD analysis of extinguished surface of sample A. Bragg-Brentano.

Table 10: quantitative analysis of A extinguished surface

Id.	Oblique beam	Bragg-Brentano
NH_4ClO_4	72%	66%
α-NH_4Cl	2%	0%
Al^0	26%	34%

Table 11: quantitative analysis of B extinguished surface

Id.	Oblique beam	Bragg-Brentano
NH_4ClO_4	58%	62%
α-NH_4Cl	1%	0%
Al^0	41%	38%

5. Final remarks

The powders presented to the reader show some properties representing indexes of material variability. Both ICP and XRD are showing some sort of peculiarities. The ICP showed some chemical contamination of other metals. These materials are contained in the bulk but the concentration is in the order of some ppm to some hundreds of ppm. The

DOI: 10.13009/EUCASS2017-674

XRD shows the possible presence of a different iron oxide (magnetite). Despite such differences, the thermal and the combustion behaviors of propellants containing the additives are overlapped and included within the band of variability. In some cases, the error bars are widened by some deficiency in material dispersion, showing indirectly the different attitude between the materials. In this respect, cohesive clustering appears to be a very important parameter for the application of a propellant catalyst and deserves a specific consideration and further analysis.

References

1. J.P. Sutton and O. Biblarz. Rocket Propulsion Elements, Seventh Edition, Wiley, 2001

2. S. Chakravarty et al. Mechanism of Burning Rate Enhancement of Composite Solid Propellants by Ferric Oxide. Journal of Propulsion and Power, 13(4):471-480, 1997

3. R.M. Cornell and U. Schwertmann. The Iron Oxides, Second Edition, Wiley-VCH, Weinheim, 2003

4. G.A.R. Guivar et al. Structural and Magnetic Properties of Monophasic Maghemite (γ-Fe2O3) Nanocrystalline. Powder, Advances in Nanoparticles, 3, 114-121, 2014

5. L. Blaney, Magnetite (Fe3O4): Properties, Synthesis, and Applications. Leigh Review, Vol. 15, Paper 5, Leigh University, 2007

6. Z. Ma et al. Effect of Fe2O3 in Fe2O3/AP Composite Particles on Thermal Decomposition of AP on Burning Rate of the Composite Propellant. Propellants, Explosives, Pyrotechnics, 31(6):447-451, 2006

7. S.S. Joshi et al. Thermal Decomposition of Ammonium Perchlorate in the Presence of Nanosized Ferric Oxide. Defence Science Journal, 58(6): 721-727, 2008

8. W. Wang and J. Yao. Catalytic Activity of Magnetite with Different Shapes for the Thermal Decomposition of Ammonium Perchlorate. Chemistry Letters, 43(10):1554:1556, 2014

9. Y. Oyumi. Plateau Burning Characteristics of AP Based Azide Composite Propellants. Propellants, Explosives, Pyrotechnics 20:150-155, 1995

10. P.R. Patil et al. Differential Scanning Calorimetry Study of HTPB based Composite Propellants in Presence of Nano Ferric Oxide. Propellant Explosives Pyrotechnics, 31(6):442-446, 2006

11. R.A. Frederick Jr. et al. Regression Rates Study of Mixed Hybrid Propellants. Journal of Propulsion and Power, 23(1):175-180, 2013

12. X. Liu, et al. Recent Studies of Decomposition and Strategies of Smoke and Toxicity Suppression for Polyurethane-based Materials. RSC Adv., In Press, 2016, DOI: 10.1039/C6RA14345H

13. J.A Puszynski. Processing and Characterization of Aluminum-based Nanothermites. Journal of Thermal Analysis and Calorimetry, 96(3):677–685, 2009

14. L. Duraes et al. Fe2O3/Aluminum Thermite Reaction Intermediate and Final Products Characterization. Materials Science and Engineering A 465:199–210, 2007

15. V.P. Zhdaov. Impact of Surface science on the Understanding of kinetics of hetergeneous Catalytic Reactions. Surface Science, 500:966-985, 2002

16. J.H. Sinfelt. Role of Surface Science in Catalysis. Catalytic Reactions. Surface Science, 500:923-946, 2002

17. AA.VV. Chemical composition. In: Springer Book of Materials Measurement Methods. Chapter 4. Eds: H. Czichos et al., Springer Science and Business Media, 2006

18. S. Brunauer et al. Adsorption of Gases in Multimolecular Layers. Journal of the American Chemical Society, 60 (2): 309–319, 1938.

19. Resodyn LabRAM, http://resodynmixers.com/products/labram/, last visit 06 Dec 16.

20. W.W. Wendlandt, Thermal Analysis, Third Edition, Wiley, 1986.